JACS
JOURNAL OF THE AMERICAN CHEMICAL SOCIETY
pubs.acs.org/JACS
Article

Mixed-Orbital Charge Transport in N-Shaped Benzene- and Pyrazine-Fused Organic Semiconductors

Craig P. Yu, Shohei Kumagai, Tomokatsu Kushida, Masato Mitani, Chikahiko Mitsui, Hiroyuki Ishii, Jun Takeya, and Toshihiro Okamoto*

Cite This: J. Am. Chem. Soc. 2022, 144, 11159−11167
Read Online
ACCESS | Metrics & More | Article Recommendations | Supporting Information

ABSTRACT: The hole-carrier transport of organic semiconductors is widely known to occur via intermolecular orbital overlaps of the highest occupied molecular orbitals (HOMO), though the effect of other occupied molecular orbitals on charge transport is rarely investigated. In this work, we first demonstrate evidence of a mixed-orbital charge transport concept in the high-performance N-shaped decyl-dinaphtho[2,3-*d*:2′,3′-*d*′]benzo[1,2-*b*:4,5-*b*′]-dithiophene (C_{10}−DNBDT−NW), where electronic couplings of the second HOMO (SHOMO) and third HOMO (THOMO) also contribute to the charge transport. We then present the molecular design of an N-shaped bis(naphtho[2′,3′:4,5]thieno)[2,3-*b*:2′,3′-*e*]pyrazine (BNTP) π-electron system to induce more pronounced mixed-orbital charge transport by incorporating the pyrazine moiety. An effective synthetic strategy for the pyrazine-fused extended π-electron system is developed. With substituent engineering, the favorable two-dimensional herringbone assembly can be obtained with BNTP, and the decylphenyl-substituted BNTP (C_{10}Ph−BNTP) demonstrates large electronic couplings involving the HOMO, SHOMO, and THOMO in the herringbone assembly. C_{10}Ph−BNTP further shows enhanced mixed-orbital charge transport when the electronic couplings of all three occupied molecular orbitals are taken into consideration, which results in a high hole mobility up to 9.6 $cm^2\ V^{-1}\ s^{-1}$ in single-crystal thin-film organic field-effect transistors. The present study provides insights into the contribution of HOMO, SHOMO, and THOMO to the mixed-orbital charge transport of organic semiconductors.

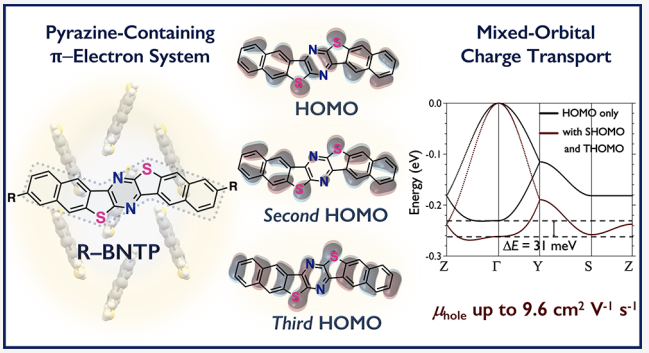

INTRODUCTION

Organic semiconductors (OSCs) held by weak van der Waals intermolecular interactions are ideal materials for flexible, thin, and lightweight next-generation electronics.[1−4] In recent years, state-of-the-art hole-transporting p-type OSCs developed by rational molecular designs have demonstrated outstanding charge-carrier mobilities (μ) over 10 $cm^2\ V^{-1}\ s^{-1}$ in solution-processed single-crystal organic field-effect transistors (OFETs),[5−9] well exceeding that of amorphous inorganic semiconductors. Among a handful of high-performance p-type OSCs that are reliably evaluated, decyl-dinaphtho[2,3-*d*:2′,3′-*d*′]benzo[1,2-*b*:4,5-*b*′]dithiophene (C_{10}−DNBDT−NW)[10] with the N-shaped geometry demonstrates high hole μ up to 16 $cm^2\ V^{-1}\ s^{-1}$, enabling the fabrication of high-frequency logic circuits using large-area solution-processed single-crystal thin films.[11−13] In light of the high performance of C_{10}−DNBDT−NW, several experimental and theoretical studies have been carried out to understand its charge-transport properties. The band-like charge transport behavior is experimentally observed in C_{10}−DNBDT−NW single-crystal thin films due to its effective intermolecular orbital overlaps.[14] The unconventional N-shaped geometry of C_{10}−DNBDT−NW with a low degree of freedom compared to the linear-shaped π-electron systems likely results in a low degree of dynamic disorder, which has been revealed to be detrimental to charge transport.[15−17] A study reported by Troisi and co-workers suggests that C_{10}−DNBDT−NW forming the two-dimensional (2D) herringbone molecular assembly in the solid state exhibits isotropic intermolecular orbital overlaps, quantified by balanced transfer integral (t) values, making it resilient to dynamic disorders compared to OSC systems with more unbalanced t.[18]

A recent report using the tight-binding approximation suggests that the high μ of [1]benzothieno[3,2-*b*][1]-benzothiophene (BTBT)[7,19] derivatives are associated with the contribution of their second highest occupied molecular orbitals (SHOMO) charge transport, in addition to the highest occupied molecular orbitals (HOMO) couplings.[20] This is

Received: February 3, 2022
Published: June 15, 2022

https://doi.org/10.1021/jacs.2c01357
J. Am. Chem. Soc. 2022, 144, 11159−11167

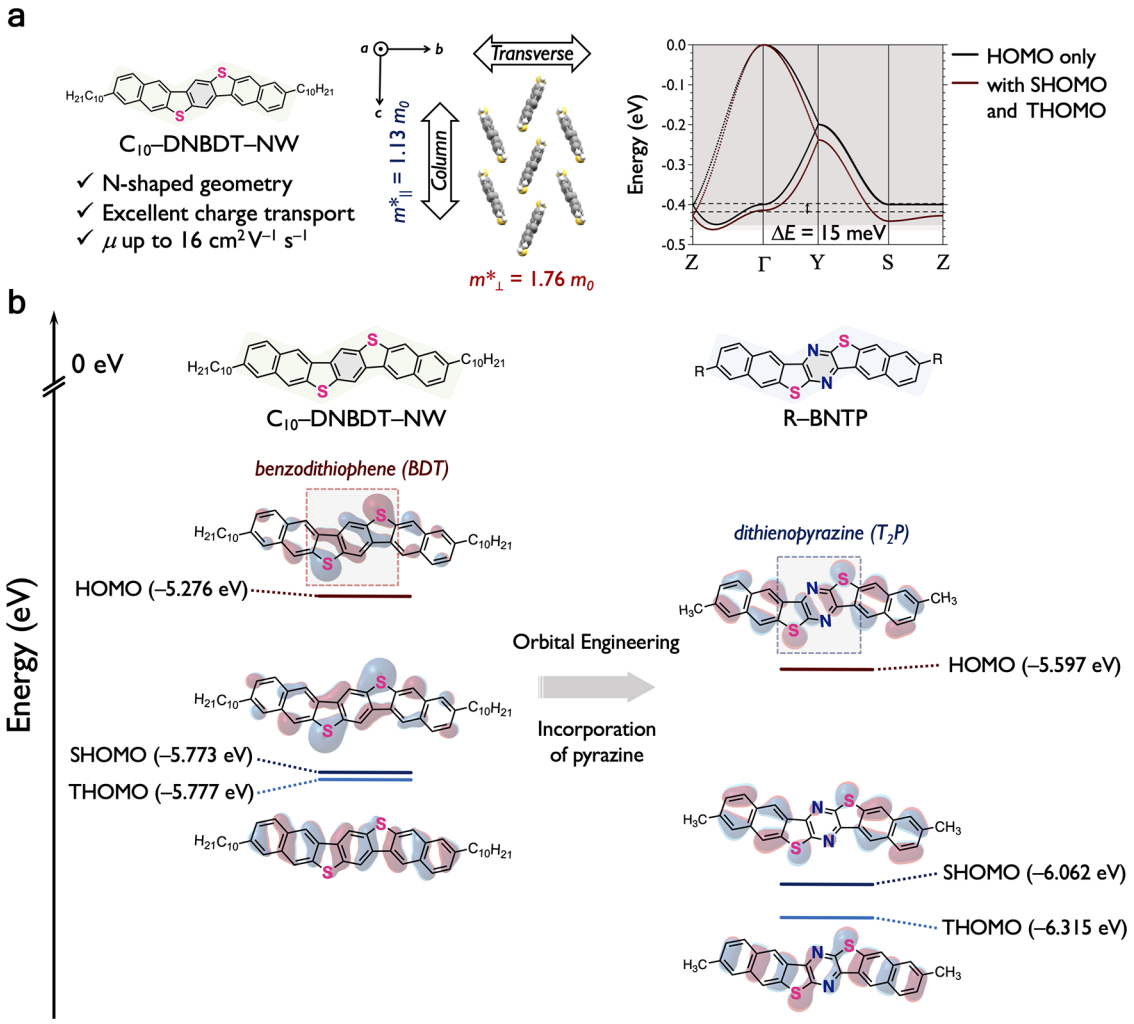

Figure 1. (a) Molecular features and herringbone assembly of C_{10}−DNBDT−NW, band structures (colored shades illustrate the bandwidths) and charge-transport capabilities estimated by the tight-binding approximation. (b) Molecular orbital distributions of C_{10}−DNBDT−NW (based on the previously reported single-crystal structure) and Me−BNTP (optimized) calculated at the B3LYP/6-311G(d) level of theory.

attributed to the small energy difference of ca. 0.4 eV between the HOMO and SHOMO levels, and large t between HOMO−SHOMO electronic couplings. By just considering the HOMO−HOMO electronic couplings, octyl-substituted BTBT (C_8−BTBT) exhibits a flat valence band maximum with small dispersion due to small t values of HOMO−HOMO in certain crystallographic directions, which is unfavorable for hole transports. When the SHOMO is incorporated in the band calculation, the curvature of the valence band maximum is drastically increased, resulting in a smaller effective mass (m^*) of hole carriers than that without SHOMO couplings; m^* is an important parameter for high-performance OSCs exhibiting band-like charge transport,[21−25] which is inversely proportional to μ (as well as t) described by the following equation, where q is the elemental charge and τ is the relaxation time.

$$\mu = q\frac{\tau}{m^*} \tag{1}$$

Since m^* is obtained from either the valence maximum or the conduction band minimum, described as

$$\frac{1}{m^*} = \frac{1}{\hbar^2}\frac{\partial^2 E}{\partial k^2} \tag{2}$$

where $\hbar$ is the Dirac's constant, E is the valence band energy, and k is the wavevector, a change in the curvature of the valence band maximum would lead to a different m^* of hole carriers.

In view of the energetic proximity of SHOMO and the third highest occupied molecular orbital (THOMO) levels of C_{10}−DNBDT−NW[26] ($E_{SHOMO} - E_{THOMO}$ = 0.004 eV), we anticipate that the THOMO may also participate in the charge transport, in addition to HOMO and SHOMO. Using the tight-binding approximation, we discover that the curvature of the valence band maximum when the electronic couplings of HOMOs, SHOMOs, and THOMOs are taken into consideration, is notably increased compared to that with electronic couplings of only HOMOs (Figures 1a and S1). Our understanding of charge transport in OSC systems is largely based on frontier orbitals, where the hole transport is conducted via HOMO overlaps for p-type, and electron transport via the lowest unoccupied molecular orbital (LUMO) overlaps for n-type OSCs. The current results strongly suggest that the SHOMO and THOMO electronic couplings in C_{10}−DNBDT−NW increase the curvature of the valence band maximum, leading to small m^* and a mixed-orbital charge transport. Thus, electronic couplings involving

https://doi.org/10.1021/jacs.2c01357
J. Am. Chem. Soc. 2022, 144, 11159−11167

Scheme 1. Synthetic Route of BNTP Derivatives[a]

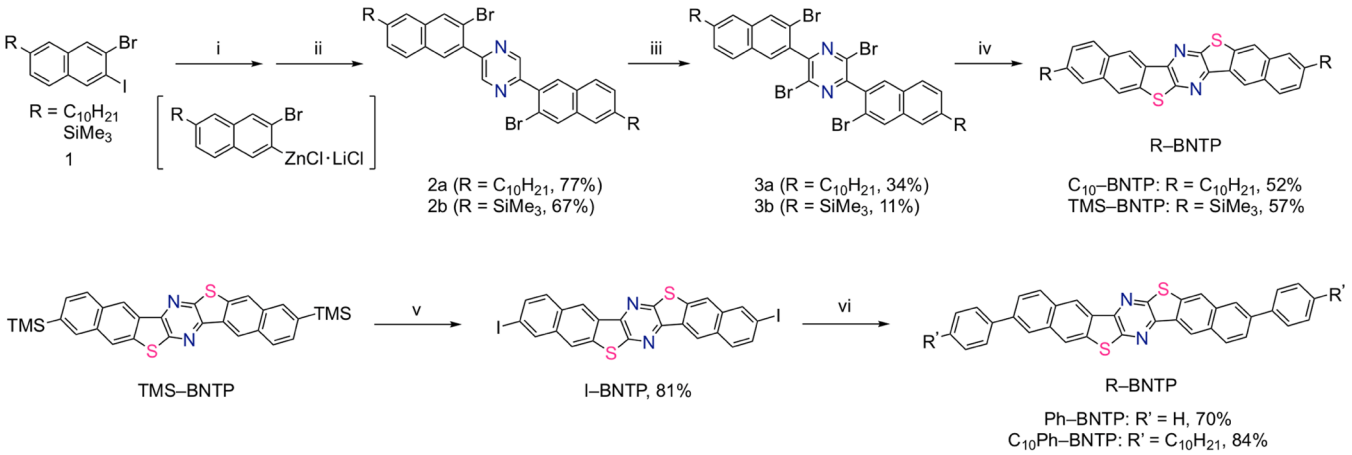

[a]Reagents and conditions: (i) iPrMgBr, $ZnCl_2$, −78 °C to r.t., LiCl, THF. (ii) 2,5-dibromopyrazine, $Pd(dba)_2$, P(2-furyl)$_3$, THF, r.t., 19 h. (iii) (1) *t*BuZn(TMP)Li, 0 °C, (2) $BrCCl_2CCl_2Br$, 0 °C, 20 h. (iv) (1) *n*BuLi, THF, −78 °C, (2) PhO_2S-S-SO_2Ph, THF, −78 °C to r.t., 12 h. (v) ICl, *o*DCB, −78 to 80 °C, 1.5 h. (vi) Ph−BNTP: (1) PhMgBr, $ZnCl_2$, LiCl, 0 °C to r.t., (2) I−BNTP, $Pd(dppf)Cl_2$, toluene, 110 °C, 12 h. C_{10}Ph−BNTP: (1) C_{10}PhBr, *n*BuLi, $ZnCl_2$, −78 °C, (2) I−BNTP, $Pd(dppf)Cl_2$, toluene, 110 °C, 12 h.

SHOMOs and THOMOs should also be examined to fully understand the charge transport of OSCs.

In this work, we envisage a substitution of the central benzene ring of DNBDT with a pyrazine moiety for a new N-shaped bis(naphtho[2′,3′:4,5]thieno)[2,3-*b*:2′,3′-*e*]pyrazine (BNTP) π-core to induce enhanced electronic couplings of HOMOs, SHOMOs, and THOMOs (Figure 1b). The pyrazine moiety has been extensively employed as a π-linker for tuning the electronic property and intramolecular charge transfer.[27−29] Molecular design of various electron-transporting n-type OSCs also involves pyrazine to achieve electron affinities for n-type device operations.[30−32] However, the pyrazine unit has not been extensively explored for p-type OSC designs due to its electron-deficient properties. Although pyrazine is shown to be effective in tuning the HOMO−LUMO energy levels, its effect on HOMO, SHOMO, and THOMO engineering, as well as hole-carrier transports, remains elusive. From our preliminary calculations, the methyl-substituted BNTP (Me−BNTP) shows large HOMO, SHOMO, and THOMO coefficients and orbital distributions on the sulfur atoms and the dithienopyrazine (T_2P) moiety (Figure 1b), which may be promising for inducing mixed-orbital charge transport. Herein, the novel R−BNTP π-core with different substituents is successfully synthesized, and a strong substituent effect is observed in their molecular assemblies. The decylphenyl-substituted BNTP (C_{10}Ph−BNTP) shows large protruding HOMO, SHOMO, and THOMO coefficients on its sulfur atoms and the T_2P moiety that are favorable for effective electronic couplings. The 2D herringbone molecular assembly of C_{10}Ph−BNTP exhibits a pronounced increased curvature of the valence band maximum when the effects of HOMO, SHOMO, and THOMO electronic couplings are incorporated in the band estimation, leading to a small m^*. The solution-processed thin film of C_{10}Ph−BNTP demonstrates high μ up to 9.6 $cm^2\ V^{-1}\ s^{-1}$, which is a new addition to the class of high-performance p-type OSCs that are applicable for high-end organic electronics. Our current results provide valuable insights into future molecular design and investigations of mixed-orbital charge transport in OSCs.

RESULTS AND DISCUSSION

Synthesis. Strategies to synthesize pyrazine-containing π-electron systems often involve condensation reactions and Buchwald−Hartwig cross-coupling of diamine groups.[33,34] However, we found that these methods were not applicable for the synthesis of BNTP due to the unique reactivity of thiophene. Hence, we developed a novel synthetic strategy for the pyrazine-containing sulfur-bridged R−BNTP in the current work (Scheme 1). From the previously synthesized compound **1**, we performed a selective halogen exchange of the aryl iodide at −78 °C to generate the organozinc intermediate *in situ*. Then, a palladium-catalyzed Negishi cross-coupling using P(2-furyl)$_3$ as the ligand[35] was done to generate the pyrazine compound **2** at room temperature in 67−77% yields. Bromination of the pyrazine core was difficult, and we discovered that the sequential use of the bulky $tBu_2Zn(TMP)$-Li[36] and $BrCCl_2CCl_2Br$[37] brominating reagent was able to selectively brominate the 2,5-positions of pyrazine to give compound **3** in 11−34% yields. Lithium-halogen exchange was performed at four aryl bromide sites of **3**, and the intramolecular annulation reaction was completed via a nucleophilic attack by the tetralithiated intermediate on benzenesulfonic thioanhydride as the source of sulfur. C_{10}− and TMS−BNTP derivatives were furnished in 52 and 57% yields, respectively. Further derivatization of the BNTP π-core started from TMS−BNTP, where the desilyliodination was directly performed by ICl at 80 °C to afford I−BTNP in 81% yield. Two more derivatives, Ph−BNTP and C_{10}Ph−BNTP, were synthesized from the versatile I−BNTP precursor by Negishi cross-coupling using $Pd(dppf)Cl_2$ in 70 and 84% yields, respectively.

Fundamental Properties. The ionization potential (IP) of C_{10}−BNTP is measured to be 5.81 eV by photoelectron yield spectroscopy (Figure S15), which is larger than that of C_{10}−DNBDT−NW (5.24 eV)[10] due to the electron-withdrawing effect of the pyrazine moiety. The film-state UV−vis spectroscopy of C_{10}−BNTP shows a red-shifted λ_{max} of 478 nm (Figure S18) relative to C_{10}−DNBDT−NW (445 nm).[9] The IP of Ph− and C_{10}Ph−BNTP are measured to be 5.55 and 5.52 eV, respectively, which are smaller than that of C_{10}−

https://doi.org/10.1021/jacs.2c01357
J. Am. Chem. Soc. 2022, 144, 11159−11167

BNTP due to the substituent effect (Figures S16 and S17). Thin-film UV−vis absorption of Ph− and C_{10}Ph−BNTP demonstrate λ_{max} of 488 and 504 nm, respectively (Figures S19 and S20). The thermal stability of C_{10}−BNTP is slightly reduced compared to C_{10}−DNBDT−NW, demonstrated by their 5% weight loss (T_{95}) of 377 °C (Figure S21) and 426 °C from the thermogravimetric analysis (TGA), respectively. However, by substituting the BNTP π-core with phenyl and decylphenyl groups, Ph− and C_{10}Ph−BNTP exhibit increased T_{95} of 469 and 440 °C, respectively (Figures S22 and S23). From the differential scanning calorimetry (DSC) profiles, we observe a low-temperature phase transition peak at 49 °C for C_{10}−BNTP, whereas C_{10}Ph−BNTP demonstrates a stable crystalline phase up to 270 °C, and Ph−BNTP shows no phase transition peaks up to 350 °C (Figures S24−S26). The solubility of C_{10}−BNTP in *o*-dichlorobenzene is 0.095 wt % at 60 °C, which is 2.2 times higher than that of C_{10}−DNBDT−NW (0.042 wt %). C_{10}Ph−BNTP also shows a higher solubility of 0.052 wt % than C_{10}−DNBDT−NW, which indicates good solution processability of BNTP derivatives (Table S1).

Single-Crystal Structures. The solution-grown single crystals of C_{10}−BNTP appear as thin yellow needles. C_{10}−BNTP crystallizes in the monoclinic *C*2/*c* space group, and in contrast to C_{10}−DNBDT−NW, the former assumes a one-dimensional (1D) π−π stacking motif with standing alkyl chains (Figure 2a). The C_{10}−BNTP π-core shows a completely planar geometry, different from the bent-shaped geometry of C_{10}−DNBDT−NW, and a large core-to-core intermolecular distance of 3.42 Å in the π−π stacking direction. The alkyl chains of C_{10}−BNTP form a large torsion angle of 110.1° with the BNTP π-core and disrupt intermolecular orbital overlaps in the π−π stacking direction.

By changing the substituents on BNTP, we observe polymorphism on Ph−BNTP that forms both needle- and plate-like single crystals. The isolated needle-like crystals (Ph−BNTP-*1D*) again exhibit the 1D π−π stacking motif, with slightly improved edge-to-face C−H···π interactions (Figure 2b). Interestingly, the plate-like crystals of Ph−BNTP (Ph−BNTP-*2D*) on the other hand, form a bent-shaped geometry with a dihedral angle of 6.5° between the planes of naphthalene and pyrazine. The dihedral angles between the phenyl ring and the BNTP π-core are measured to be 41.8 and 26.5° for Ph−BNTP-*1D* and Ph−BNTP-*2D*, respectively. The molecular assembly of Ph−BNTP shows a 2D herringbone assembly, where the angle between planes of dimers (defined as the herringbone angle) is measured to be 38° (Figure 2c).

After examining the above single-crystal structures of BNTP derivatives, it is apparent that the 2D herringbone assembly can be induced by enhanced intermolecular interactions. We subsequently employed the decylphenyl substituent to stabilize the herringbone assembly and obtained isomorphic crystal structure by increasing the total van der Waals forces from the introduction of alkyl chains.[25] Indeed, C_{10}Ph−BNTP forms exclusively large yellow plate-like single crystals, and the structure exhibits a bent geometry, with a bent angle of 7.0°, likely induced by the enhanced intermolecular interactions (Figure 2d). The phenyl rings of C_{10}Ph−BNTP form a small dihedral angle of 14.9° with the bonded naphthalene, and the decyl alkyl chains are laterally extended, which is drastically different from C_{10}−BNTP. The 2D herringbone motif is adopted by C_{10}Ph−BNTP, with a herringbone angle of 49°.

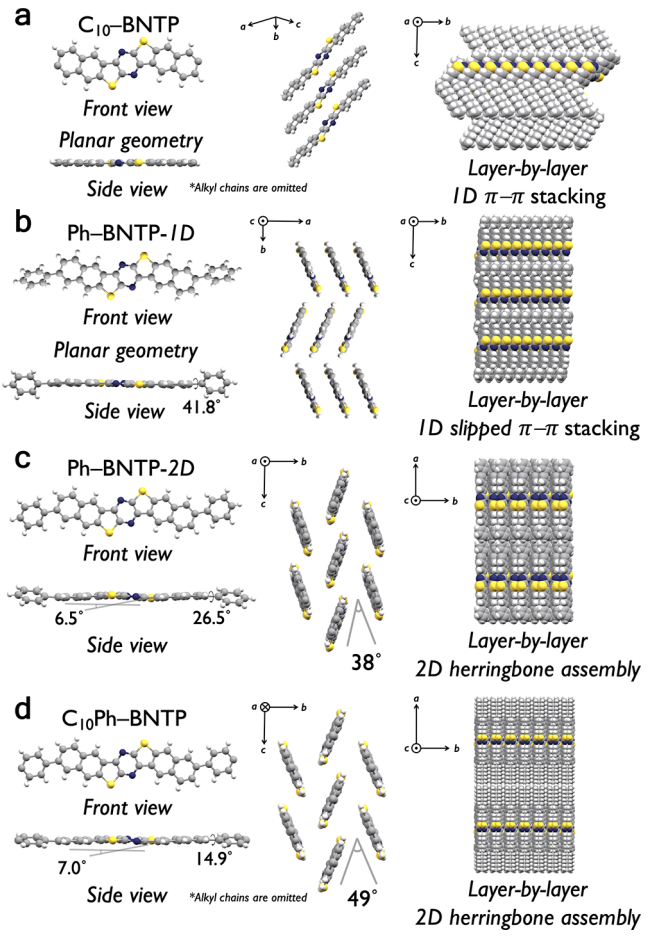

Figure 2. Molecular geometry, bent angle, packing motif (substituents omitted for clarity), and interlayer molecular assembly of (a−d) C_{10}−, Ph- (1D and 2D), and C_{10}Ph−BNTP, respectively, in the single-crystal structures obtained at ambient temperatures.

Estimation of Transfer Integrals. From the molecular assemblies of R−BNTP, *t* values of HOMO−HOMO electronic couplings are calculated at the PBEPBE/6-31G(d) level to estimate their charge-transport capabilities.[38] The 1D π−π stacking of C_{10}−BNTP shows a large core-to-core distance in the *b*-axis direction that results in a *t* value of −20 meV and no significant intermolecular orbital overlaps in the *c*-axis direction, indicating a 1D charge-transport behavior (Figure 2a). Similarly, the major charge transport of Ph−BNTP-*1D* is contributed by the face-to-face π−π stacking along the *a*-axis direction with a *t* value of +14.9 meV, while *t* values from the edge-to-face interactions are −2.23 and −0.236 meV (Figure 2b). Charge transport of the herringbone molecular assembly can be quantified as

$$\frac{1}{m^*} = \frac{1}{\hbar^2} d^2 (2t_{column} + |t_{trans}|) \quad (3)$$

where *d* is the lattice constant in the column direction and t_{column} and $|t_{trans}|$ are the transfer integrals in the column and transverse directions, respectively. Here, the sign of t_{column} is important, with the positive *t* value (overlaps with the opposite phases of molecular orbitals) being favorable for charge transport and *vice versa*, while only the absolute value of t_{trans} is important. For Ph−BNTP-*2D* and C_{10}Ph−BNTP that form the herringbone assembly, we define their t_{column} as $t_{1,4}$, and their $|t_{trans}|$ as $|t_{2,3,5,6}|$ as shown in Table S3. Since single-crystal

https://doi.org/10.1021/jacs.2c01357
J. Am. Chem. Soc. 2022, 144, 11159−11167

structures of Ph−BNTP-*2D*, C_{10}Ph−BNTP, and C_{10}−DNBDT−NW have similar lattice constants in the column direction, ranging from 6.11 to 6.51 Å, their charge transports can be effectively studied with *t* values.

Here, we show all *t* values of Ph−BNTP-*2D*, C_{10}Ph−BNTP, and C_{10}−DNBDT−NW (as reference) involving HOMO, SHOMO, and THOMO (Table S3) to investigate their mixed-orbital charge-transport capabilities. Based on the previous report, the sign of transfer integrals in the transverse direction becomes important in investigating the mixed-orbital charge transport.[20] Although Ph−BNTP-*2D* exhibits a 2D herringbone assembly, the small herringbone angle of 38° in combination with its HOMO distribution results in ineffective intermolecular orbital overlap in the column direction (*c*-axis) that is indicated by $t_{1,4}$ of +6.90 meV, but the transverse direction (*b*-axis) shows large $|t_{2,3,5,6}|$ of 47.9 meV. Ph−BNTP-*2D* shows a much smaller *t* value of +0.131 meV from HOMO−SHOMO couplings in the column direction, suggesting that the SHOMO may have small contributions to its charge transport. By calculating *t* values from HOMO−THOMO couplings, $t_{1,4}$ increases to −8.93 meV in the column direction, $t_{2,5}$ and $t_{3,6}$ also show large values of −42.9 and −42.3 meV, respectively, in the transverse directions. The *t* values of HOMO, SHOMO, and THOMO of Ph−BNTP-*2D* here suggest that the electronic couplings from these orbitals should be fully investigated for understanding the charge transport of OSCs.

The 2D charge-transport capability is apparent in C_{10}Ph−BNTP as the column direction (*c*-axis) shows an enhanced $t_{1,4}$ of +16.6 meV, and the transverse direction also exhibits large $|t_{2,3,5,6}|$ of 28.8 meV (Table S3). Similar to Ph−BNTP-*2D* and C_{10}−DNBDT−NW, C_{10}Ph−BNTP shows smaller *t* values in the column directions from HOMO−SHOMO couplings than those from HOMO−HOMO couplings. However, C_{10}Ph−BNTP demonstrates $t_{1,4}$ of −14.9 meV from HOMO−THOMO couplings. In addition, the transverse directions of C_{10}Ph−BNTP exhibit large $t_{2,5}$ and $t_{3,6}$ of −46.3 and −49.0 meV from HOMO−THOMO compared to its HOMO−HOMO couplings in the transverse directions. The results herein indicate a significant contribution of HOMO, SHOMO, and THOMO electronic couplings in Ph−BNTP-*2D* and C_{10}Ph−BNTP.

The fascinating electronic couplings of current BNTP derivatives may be potentially attributed to two reasons. For instance, the small energy differences between HOMO−SHOMO and HOMO−THOMO levels of C_{10}Ph−BNTP are calculated to be 0.51 and 0.64 eV, respectively, based on the geometry of its single-crystal structure (Figure 3). We propose that OSCs with an energy difference around 0.6 eV between HOMO, SHOMO, and THOMO may be considered for the mixed-orbital charge transport. Note that the orbital energies calculated using the single-crystal structure may be different from those of the optimized structure due to the effect of molecular packings. Similar to C_{10}−DNBDT−NW, the energy difference between SHOMO and THOMO levels of C_{10}Ph−BNTP is only 0.13 eV. We postulate that such energetic proximity of these three occupied molecular orbitals allows them to participate in electronic couplings and contribute to the charge transport. Another factor may be attributed to the molecular orbital distributions of BNTP. The single-crystal structure of C_{10}Ph−BNTP shows large HOMO distribution on the sulfur atoms as well as the T_2P moiety, which may strongly contribute to the electronic couplings in both the column and

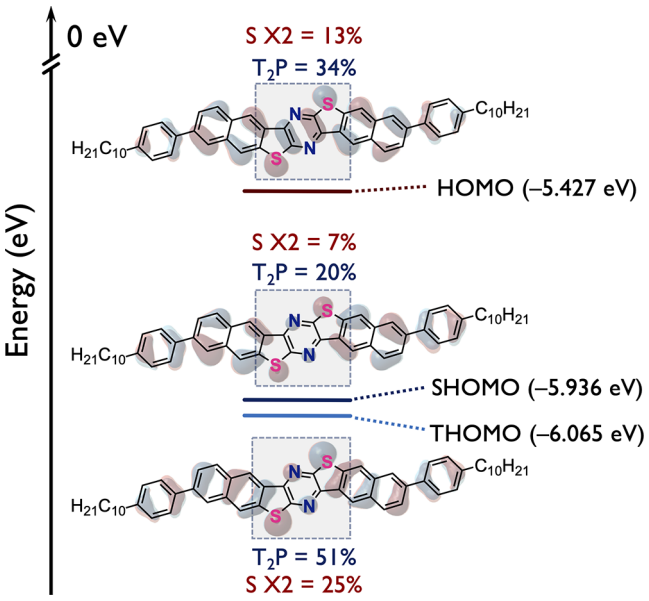

Figure 3. Distribution of HOMO, SHOMO, and THOMO of C_{10}Ph−BNTP calculated at the B3LYP/6-311G(d) level of theory using the single-crystal structures. Orbital composition analysis was performed with the Mulliken partition using the Multifwn program.[39]

transverse directions.[9] Large SHOMO and THOMO distributions are also observed on these units that participate in the electronic couplings through effective intermolecular orbital overlaps. Similarly, C_{10}−DNBDT−NW and Ph−BNTP both exhibit large molecular orbital distributions on sulfur and central BDT and T_2P moieties (Figure S27).

Estimation of Effective Masses. To further investigate the charge-transport capability of BNTP derivatives, we performed band structure and m^* (in units of m_0: the rest mass of an electron) calculations via the plane-wave basis.[40] Derivatives C_{10}−BNTP and Ph−BNTP-*1D* with 1D assemblies give negligible valence band dispersions and large m^* values that are unfavorable for charge transport (Figure S31). Both Ph−BNTP-*2D* and C_{10}Ph−BNTP with the 2D herringbone assembly demonstrate large curvature of valence bands at the Γ point, resulting in small $m^*_{\parallel}$ values of 1.54 and 1.43 m_0, respectively, in the column direction, and $m^*_{\perp}$ of 1.70 and 1.91 m_0, respectively, in the transverse direction (Figure 4a,b). The small m^* values of Ph−BNTP-*2D* and C_{10}Ph−BNTP [comparable to those of C_{10}−DNBDT−NW (Figure 1a)] are intriguing considering that their *t* values from HOMO−HOMO couplings are not as large as C_{10}−DNBDT−NW. Since both derivatives exhibit large SHOMO and THOMO bandwidths and overlaps between these bands (Figure 4a,b), we postulate that their band structures estimated from the plane-wave basis contain significant contributions from SHOMO and THOMO in addition to HOMO.

With the tight-binding approximation, we are able to separately examine the effects of only HOMO couplings, as well as combined HOMO, SHOMO, and THOMO couplings on the curvature of valence band maxima. For C_{10}−DNBDT−NW, the curvature of the valence band maximum from only HOMO−HOMO electronic couplings at the Γ point is different from that when all HOMO, SHOMO, and THOMO electronic couplings are taken into consideration in the tight-binding approximation. The effect of orbital hybridization can be preliminarily expressed by the energy

https://doi.org/10.1021/jacs.2c01357
J. Am. Chem. Soc. 2022, 144, 11159−11167

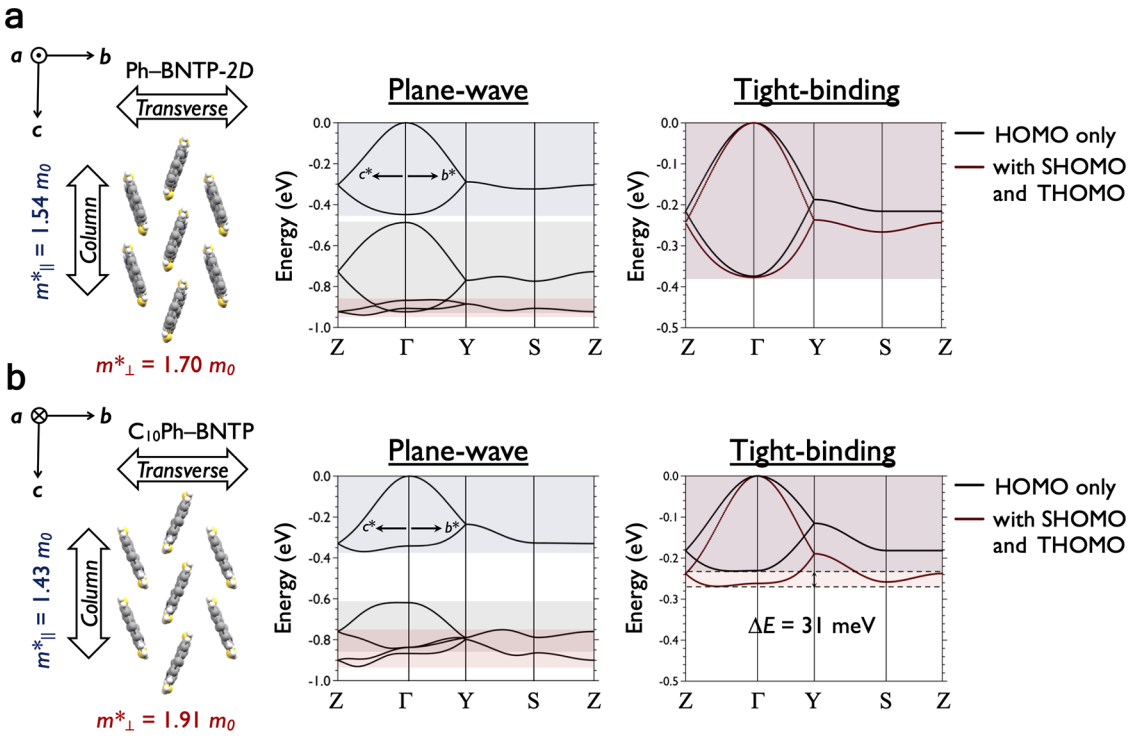

Figure 4. Band structures (colored shades illustrate the bandwidths) and effective masses of (a) Ph–BNTP-*2D* and (b) C_{10}Ph–BNTP obtained using the plane-wave (c* and b* correspond to the column and transverse directions in the herringbone packing) and tight-binding approximations calculated at the PBEPBE/6-31G(d) level of theory.

difference (ΔE, determined by both the sign and magnitude of transfer integrals)[20] of the bands at the Γ point, which is 15 meV for C_{10}–-DNBDT–NW (Figure 1a), but it is minuscule for Ph–BNTP-*2D* (Figure 4a). In the case of C_{10}Ph–BNTP, incorporating the HOMO, SHOMO, and THOMO electronic couplings in the calculation drastically increases the curvature of the valence band maximum at the Γ point, which is accompanied by a significant increase in the ΔE of 31 meV (Figure 4b), suggesting an effect of the mixed-orbital charge transport.

We observe that the m^* values of Ph– and C_{10}Ph–BNTP in the column direction (Γ–*Z*) are significantly reduced from the increased curvature of their valence band maxima as the electronic couplings of SHOMO and THOMO are considered (Table S4). A similar reduction of m^* in the column direction is observed in C_{10}–DNBDT–NW with the incorporation of orbital hybridizations (Table S4), though to a lesser degree than that of C_{10}Ph–BNTP. The tight-binding approximation suggests that the mixed-orbital phenomenon is present in C_{10}–DNBDT–NW, Ph–BNTP-*2D*, and C_{10}Ph–BNTP, while C_{10}Ph–BNTP shows the strongest contribution from the electronic couplings of HOMO, SHOMO, and THOMO to its charge-transport capability.

OFET Performances. Bottom-gate/top-contact OFETs are fabricated with R–BNTP derivatives as the active layer to experimentally evaluate their charge-transport capabilities. The single-crystal thin films of C_{10}–BNTP (Figure S28) fabricated by the edge-casting method[41] show no apparent semiconductor behavior (Figure S32a,c), which is reasonable considering its unfavorable molecular assembly, intermolecular orbital overlaps, and the negligible dispersion of valence band structure. Interestingly, Ph–BNTP-*2D* crystals can be exclusively obtained by the physical vapor transport (PVT) method, and the plate-like crystals are manually laminated on OFET substrates. The OFET channels are constructed along the column direction (*c*-axis) (Figure S29) of the Ph–BNTP-*2D* single crystals, and the highest μ is measured to be 0.8 $cm^2 V^{-1} s^{-1}$ (Figure S32b,d). Despite the 2D herringbone assembly, Ph–BNTP-*2D* shows small *t* values along the column direction (channel direction), which explains its low μ.

On the other hand, C_{10}Ph–BNTP with long alkyl chains offers excellent solution processability, where large single-crystalline domains are easily formed via the solution-processed edge-casting method (Figure 5a). Its thin-film

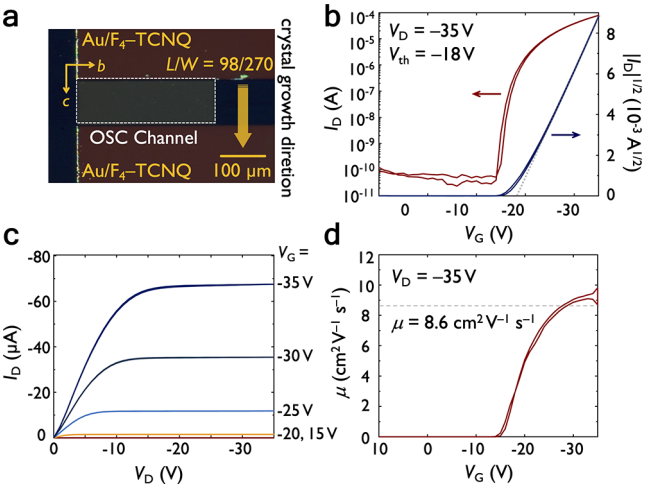

Figure 5. (a) Polarized optical microscopic image of the channel; (b) transfer characteristic, the gray dashed line illustrates the fit to $|I_D|^{1/2}$, from which the μ was estimated; (c) output characteristic; and (d) gate voltage-dependent μ of single-crystalline thin-film OFET fabricated with C_{10}Ph–BNTP on the parylene diX-SR insulating layer.

https://doi.org/10.1021/jacs.2c01357
J. Am. Chem. Soc. 2022, 144, 11159–11167

structure is consistent with its bulk single-crystalline structure, which allows us to correlate our mixed-orbital charge-transport estimations with its device performance. The OFETs with channels constructed along the column direction (*c*-axis) (Figure S30) of C_{10}Ph−BNTP exhibit excellent p-type OSC behavior (Figure 5b,c) with small hysteresis and V_{th} of −18 V, and the highest μ is measured to be 8.6 $cm^2\ V^{-1}\ s^{-1}$ (Figure 5d) on the parylene diX-SR insulating layer (averaged μ of 6.3 $cm^2\ V^{-1}\ s^{-1}$ over 17 devices (Figure S33)). C_{10}Ph-BNTP OFETs using the β-phenethyltrichlorosilane (β-PTS) dielectric layer with the same device architecture demonstrate an improved highest μ of 9.6 $cm^2\ V^{-1}\ s^{-1}$, with a V_{th} of −19 V (Figure S34). We summarize the fundamental properties and OFET performances of C_{10}−DNBDT−NW and R−BNTP derivatives in Table S5 for comparison. The μ value of C_{10}Ph−BNTP is considerable among the high-performance thienoacene-type organic semiconductors.[42] Although the current single-crystalline OFET performances of C_{10}Ph−BNTP exhibit relatively large threshold voltages and bias stress (Figure S35), further optimization of the device fabrications needs to be carried out in future work.

Despite having relatively small *t* values from HOMO−HOMO couplings, C_{10}Ph−BNTP with large SHOMO and THOMO coefficients in the central T_2P moiety exhibits large *t* values from HOMO−SHOMO and HOMO−THOMO electronic couplings. The plane-wave basis suggests a small m^* of C_{10}Ph−BNTP, and we have identified significant contributions from SHOMO and THOMO electronic couplings based on the tight-binding approximation, which indicates a mixed-orbital charge transport. The estimated charge-transport capability of C_{10}Ph−BNTP is further substantiated by the high μ in solution-processed single-crystalline thin-film OFETs.

CONCLUSIONS

In this work, we report the molecular design for mixed-orbital charge transport via HOMO, SHOMO, and THOMO engineering with a pyrazine-containing N-shaped BNTP π-core. A robust synthetic strategy is developed to synthesize various R−BNTP derivatives, which is also applicable for the synthesis of other pyrazine-containing π-electron systems. The single-crystal structure of C_{10}-BNTP adopts a 1D $\pi-\pi$ stacking that results in poor charge transport. The favorable 2D herringbone assembly is induced by introducing phenyl and decylphenyl substituents. Ph− and C_{10}Ph−BNTP both demonstrate relatively small *t* values from HOMO−HOMO couplings compared to the high-performance C_{10}−DNBDT−NW. However, the curvature of valence band maxima of Ph− and C_{10}Ph−BNTP are drastically increased when SHOMO and THOMO electronic couplings are incorporated in the band estimation, compared to those where only HOMO−HOMO couplings are considered. C_{10}Ph−BNTP with evidence of effective mixed-orbital charge transport demonstrates μ as high as 9.6 $cm^2\ V^{-1}\ s^{-1}$ in solution-processed single-crystalline thin films, which is promising for fabricating high-end organic electronics. The present study suggests that the orbital hybridization of HOMO, SHOMO, and THOMO may contribute to the formation of the valence band of OSCs, and the mixed-orbital effect should be investigated to gain a more complete understanding of the charge transport of OSCs.

ASSOCIATED CONTENT

Supporting Information

The Supporting Information is available free of charge at https://pubs.acs.org/doi/10.1021/jacs.2c01357.

Synthetic procedures, ^1H and ^{13}C NMR spectra, theoretical calculation details, physicochemical characterizations, X-ray crystallographic information, and device evaluations (PDF)

Accession Codes

CCDC 2149885−2149888 contain the supplementary crystallographic data for this paper. These data can be obtained free of charge via www.ccdc.cam.ac.uk/data_request/cif, or by emailing data_request@ccdc.cam.ac.uk, or by contacting The Cambridge Crystallographic Data Centre, 12 Union Road, Cambridge CB2 1EZ, UK; fax: +44 1223 336033.

AUTHOR INFORMATION

Corresponding Author

Toshihiro Okamoto − *Material Innovation Research Center (MIRC) and Department of Advanced Materials Science, Graduate School of Frontier Sciences, The University of Tokyo, Kashiwa, Chiba 277-8561, Japan; PRESTO, JST, Kawaguchi, Saitama 332-0012, Japan;* orcid.org/0000-0002-4783-0621; Email: tokamoto@k.u-tokyo.ac.jp

Authors

Craig P. Yu − *Material Innovation Research Center (MIRC) and Department of Advanced Materials Science, Graduate School of Frontier Sciences, The University of Tokyo, Kashiwa, Chiba 277-8561, Japan;* orcid.org/0000-0002-1423-5244

Shohei Kumagai − *Material Innovation Research Center (MIRC) and Department of Advanced Materials Science, Graduate School of Frontier Sciences, The University of Tokyo, Kashiwa, Chiba 277-8561, Japan;* orcid.org/0000-0002-1554-054X

Tomokatsu Kushida − *Material Innovation Research Center (MIRC) and Department of Advanced Materials Science, Graduate School of Frontier Sciences, The University of Tokyo, Kashiwa, Chiba 277-8561, Japan*

Masato Mitani − *Material Innovation Research Center (MIRC) and Department of Advanced Materials Science, Graduate School of Frontier Sciences, The University of Tokyo, Kashiwa, Chiba 277-8561, Japan*

Chikahiko Mitsui − *Material Innovation Research Center (MIRC) and Department of Advanced Materials Science, Graduate School of Frontier Sciences, The University of Tokyo, Kashiwa, Chiba 277-8561, Japan*

Hiroyuki Ishii − *Department of Applied Physics, Faculty of Pure and Applied Sciences, University of Tsukuba, Tsukuba, Ibaraki 305-8573, Japan;* orcid.org/0000-0003-0644-1424

Jun Takeya − *Material Innovation Research Center (MIRC) and Department of Advanced Materials Science, Graduate School of Frontier Sciences, The University of Tokyo, Kashiwa, Chiba 277-8561, Japan; International Center for Materials Nanoarchitectonics (MANA), National Institute for Materials Science (NIMS), Tsukuba 205-0044, Japan*

Complete contact information is available at: https://pubs.acs.org/10.1021/jacs.2c01357

Author Contributions

The manuscript was written through contributions of all authors. All authors have given approval to the final version of the manuscript.

Notes

The authors declare no competing financial interest.

■ ACKNOWLEDGMENTS

This work was supported by the JST-PRESTO and JST-CREST programs "Scientific Innovation for Energy Harvesting Technology" (Numbers JPMJPR17R2 and JPMJCR21Q1), "Exploring Innovative Materials in Unknown Search Space" (Number JPMJCR21O3) and by KAKENHI. C.P.Y. thanks the Grant-in-Aid for JSPS Fellows (Number JP20J12608), T.O. and H.I. thank JSPS for Grants-in-Aid for Scientific Research, B (Numbers JP17H03104 and JP18H01856).

■ REFERENCES

(1) Berggren, M.; Nilsson, D.; Robinson, N. D. Organic Materials for Printed Electronics. *Nat. Mater.* **2007**, *6*, 3−5.
(2) Rogers, J. A.; Someya, T.; Huang, Y. Materials and Mechanics for Stretchable Electronics. *Science* **2010**, *327*, 1603−1607.
(3) Someya, T.; Bao, Z.; Malliaras, G. G. The Rise of Plastic Bioelectronics. *Nature* **2016**, *540*, 379−385.
(4) Fratini, S.; Nikolka, M.; Salleo, A.; Schweicher, G.; Sirringhaus, H. Charge Transport in High-Mobility Conjugated Polymers and Molecular Semiconductors. *Nat. Mater.* **2020**, *19*, 491−502.
(5) Giri, G.; Verploegen, E.; Mannsfeld, S. C. B. B.; Atahan-Evrenk, S.; Kim, D. H.; Lee, S. Y.; Becerril, H. A.; Aspuru-Guzik, A.; Toney, M. F.; Bao, Z. Tuning Charge Transport in Solution-Sheared Organic Semiconductors Using Lattice Strain. *Nature* **2011**, *480*, 504−508.
(6) Okamoto, T.; Mitsui, C.; Yamagishi, M.; Nakahara, K.; Soeda, J.; Hirose, Y.; Miwa, K.; Sato, H.; Yamano, A.; Matsushita, T.; Uemura, T.; Takeya, J. V-Shaped Organic Semiconductors with Solution Processability, High Mobility, and High Thermal Durability. *Adv. Mater.* **2013**, *25*, 6392−6397.
(7) Iino, H.; Usui, T.; Hanna, J. Liquid Crystals for Organic Thin-Film Transistors. *Nat. Commun.* **2015**, *6*, No. 6828.
(8) Yamamoto, A.; Murata, Y.; Mitsui, C.; Ishii, H.; Yamagishi, M.; Yano, M.; Sato, H.; Yamano, A.; Takeya, J.; Okamoto, T. Zigzag-Elongated Fused π-Electronic Core: A Molecular Design Strategy to Maximize Charge-Carrier Mobility. *Adv. Sci.* **2018**, *5*, No. 1700317.
(9) Okamoto, T.; Yu, C. P.; Mitsui, C.; Yamagishi, M.; Ishii, H.; Takeya, J. Bent-Shaped p-Type Small-Molecule Organic Semiconductors: A Molecular Design Strategy for Next-Generation Practical Applications. *J. Am. Chem. Soc.* **2020**, *142*, 9083−9096.
(10) Mitsui, C.; Okamoto, T.; Yamagishi, M.; Tsurumi, J.; Yoshimoto, K.; Nakahara, K.; Soeda, J.; Hirose, Y.; Sato, H.; Yamano, A.; Uemura, T.; Takeya, J. High-Performance Solution-Processable N-Shaped Organic Semiconducting Materials with Stabilized Crystal Phase. *Adv Mater.* **2014**, *26*, 4546−4551.
(11) Yamamura, A.; Watanabe, S.; Uno, M.; Mitani, M.; Mitsui, C.; Tsurumi, J.; Isahaya, N.; Kanaoka, Y.; Okamoto, T.; Takeya, J. Wafer-Scale, Layer-Controlled Organic Single Crystals for High-Speed Circuit Operation. *Sci. Adv.* **2018**, *4*, No. eaao5758.
(12) Makita, T.; Kumagai, S.; Kumamoto, A.; Mitani, M.; Tsurumi, J.; Hakamatani, R.; Sasaki, M.; Okamoto, T.; Ikuhara, Y.; Watanabe, S.; Takeya, J. High-Performance, Semiconducting Membrane Composed of Ultrathin, Single-Crystal Organic Semiconductors. *Proc. Natl. Acad. Sci. U.S.A.* **2020**, *117*, 80−85.
(13) Sawada, T.; Yamamura, A.; Sasaki, M.; Takahira, K.; Okamoto, T.; Watanabe, S.; Takeya, J. Correlation between the Static and Dynamic Responses of Organic Single-Crystal Field-Effect Transistors. *Nat. Commun.* **2020**, *11*, No. 4839.
(14) Tsurumi, J.; Matsui, H.; Kubo, T.; Häusermann, R.; Mitsui, C.; Okamoto, T.; Watanabe, S.; Takeya, J. Coexistence of Ultra-Long Spin Relaxation Time and Coherent Charge Transport in Organic Single-Crystal Semiconductors. *Nat. Phys.* **2017**, *13*, 994−998.
(15) Eggeman, A. S.; Illig, S.; Troisi, A.; Sirringhaus, H.; Midgley, P. A. Measurement of Molecular Motion in Organic Semiconductors by Thermal Diffuse Electron Scattering. *Nat. Mater.* **2013**, *12*, 1045−1049.
(16) Illig, S.; Eggeman, A. S.; Troisi, A.; Jiang, L.; Warwick, C.; Nikolka, M.; Schweicher, G.; Yeates, S. G.; Henri Geerts, Y.; Anthony, J. E.; Sirringhaus, H. Reducing Dynamic Disorder in Small-Molecule Organic Semiconductors by Suppressing Large-Amplitude Thermal Motions. *Nat. Commun.* **2016**, *7*, No. 10736.
(17) Schweicher, G.; D'Avino, G.; Ruggiero, M. T.; Harkin, D. J.; Broch, K.; Venkateshvaran, D.; Liu, G.; Richard, A.; Ruzié, C.; Armstrong, J.; Kennedy, A. R.; Shankland, K.; Takimiya, K.; Geerts, Y. H.; Zeitler, J. A.; Fratini, S.; Sirringhaus, H. Chasing the "Killer" Phonon Mode for the Rational Design of Low-Disorder, High-Mobility Molecular Semiconductors. *Adv. Mater.* **2019**, *31*, No. 1902407.
(18) Fratini, S.; Ciuchi, S.; Mayou, D.; Trambly, L.; Troisi, A. A Map of High-Mobility Molecular Semiconductors. *Nat. Mater.* **2017**, *16*, 998−1002.
(19) Ebata, H.; Izawa, T.; Miyazaki, E.; Takimiya, K.; Ikeda, M.; Kuwabara, H.; Yui, T. Highly Soluble [1]Benzothieno[3,2-b]-Benzothiophene (BTBT) Derivatives for High-Performance, Solution-Processed Organic Field-Effect Transistors. *J. Am. Chem. Soc.* **2007**, *129*, 15732−15733.
(20) Kuroda, Y.; Ishii, H.; Yoshino, S.; Kobayashi, N. Second Highest Occupied Molecular Orbital Effects on the Valence Band Structure of Organic Semiconductors. *Jpn. J. Appl. Phys.* **2019**, *58*, No. SIIB27.
(21) Takeya, J.; Tsukagoshi, K.; Aoyagi, Y.; Takenobu, T.; Iwasa, Y. Hall Effect of Quasi-Hole Gas in Organic Single-Crystal Transistors. *Jpn. J. Appl. Phys.* **2005**, *44*, No. L1393.
(22) Podzorov, V.; Menard, E.; Rogers, J. A.; Gershenson, M. E. Hall Effect in the Accumulation Layers on the Surface of Organic Semiconductors. *Phys. Rev. Lett.* **2005**, *95*, No. 226601.
(23) Takeya, J.; Kato, J.; Hara, K.; Yamagishi, M.; Hirahara, R.; Yamada, K.; Nakazawa, Y.; Ikehata, S.; Tsukagoshi, K.; Aoyagi, Y.; Takenobu, T.; Iwasa, Y. In-Crystal and Surface Charge Transport of Electric-Field-Induced Carriers in Organic Single-Crystal Semiconductors. *Phys. Rev. Lett.* **2007**, *98*, No. 196804.
(24) Okamoto, T.; Kumagai, S.; Fukuzaki, E.; Ishii, H.; Watanabe, G.; Niitsu, N.; Annaka, T.; Yamagishi, M.; Tani, Y.; Sugiura, H.; Watanabe, T.; Watanabe, S.; Takeya, J. Robust, High-Performance n-Type Organic Semiconductors. *Sci. Adv.* **2020**, *6*, No. eaaz0632.
(25) Sawabe, C.; Kumagai, S.; Mitani, M.; Ishii, H.; Yamagishi, M.; Sagayama, H.; Kumai, R.; Sato, H.; Takeya, J.; Okamoto, T. Band-like Transporting and Thermally Durable V-Shaped Organic Semiconductors with a Phenyl Key Block. *J. Mater. Chem. C* **2020**, *8*, 14172−14179.
(26) Otaki, T.; Terashige, T.; Tsurumi, J.; Miyamoto, T.; Kida, N.; Watanabe, S.; Okamoto, T.; Takeya, J.; Okamoto, H. Evaluations of Nonlocal Electron-Phonon Couplings in Tetracene, Rubrene, and C_{10}-DNBDT-NW Based on Density Functional Theory. *Phys. Rev. B* **2020**, *102*, No. 245201.
(27) Wang, E.; Hou, L.; Wang, Z.; Hellström, S.; Zhang, F.; Inganäs, O.; Andersson, M. R. An Easily Synthesized Blue Polymer for High-Performance Polymer Solar Cells. *Adv. Mater.* **2010**, *22*, 5240−5244.
(28) Desta, M. B.; Vinh, N. S.; Pavan Kumar, C.; Chaurasia, S.; Wu, W. T.; Lin, J. T.; Wei, T. C.; Wei-Guang Diau, E. Pyrazine-Incorporating Panchromatic Sensitizers for Dye Sensitized Solar Cells under One Sun and Dim Light. *J. Mater. Chem. A* **2018**, *6*, 13778−13789.
(29) Xue, J.; Liang, Q.; Wang, R.; Hou, J.; Li, W.; Peng, Q.; Shuai, Z.; Qiao, J. Highly Efficient Thermally Activated Delayed Fluorescence via J-Aggregates with Strong Intermolecular Charge Transfer. *Adv. Mater.* **2019**, *31*, No. 1808242.
(30) Li, H.; Kim, F. S.; Ren, G.; Hollenbeck, E. C.; Subramaniyan, S.; Jenekhe, S. A. Tetraazabenzodifluoranthene Diimides: Building

https://doi.org/10.1021/jacs.2c01357
J. Am. Chem. Soc. 2022, 144, 11159−11167

Blocks for Solution-Processable n-Type Organic Semiconductors. *Angew. Chem., Int. Ed.* **2013**, *52*, 5513−5517.
(31) Liang, Z.; Tang, Q.; Xu, J.; Miao, Q. Soluble and Stable N-Heteropentacenes with High Field-Effect Mobility. *Adv. Mater.* **2011**, *23*, 1535−1539.
(32) Xu, X.; Yao, Y.; Shan, B.; Gu, X.; Liu, D.; Liu, J.; Xu, J.; Zhao, N.; Hu, W.; Miao, Q. Electron Mobility Exceeding 10 $cm^2 V^{-1} s^{-1}$ and Band-Like Charge Transport in Solution-Processed n-Channel Organic Thin-Film Transistors. *Adv. Mater.* **2016**, *28*, 5276−5283.
(33) Bunz, U. H. F.; Engelhart, J. U.; Lindner, B. D.; Schaffroth, M. Large N-Heteroacenes: New Tricks for Very Old Dogs? *Angew. Chem., Int. Ed.* **2013**, *52*, 3810−3821.
(34) Miao, Q.; Miao, Q. Ten Years of N-Heteropentacenes as Semiconductors for Organic Thin-Film Transistors. *Adv. Mater.* **2014**, *26*, 5541−5549.
(35) Andersen, N. G.; Keay, B. A. 2-Furyl Phosphines as Ligands for Transition-Metal-Mediated Organic Synthesis. *Chem. Rev.* **2001**, *101*, 997−1030.
(36) Kondo, Y.; Shilai, M.; Uchiyama, M.; Sakamoto, T. TMP-Zincate as Highly Chemoselective Base for Directed Ortho Metalation. *J. Am. Chem. Soc.* **1999**, *121*, 3539−3540.
(37) Lin, W.; Baron, O.; Knochel, P. Highly Functionalized Benzene Syntheses by Directed Mono or Multiple Magnesiations with TMPMgCl·LiCl. *Org. Lett.* **2006**, *8*, 5673−5676.
(38) Valeev, E. F.; Coropceanu, V.; da Silva Filho, D. A.; Salman, S.; Brédas, J. L. Effect of Electronic Polarization on Charge-Transport Parameters in Molecular Organic Semiconductors. *J. Am. Chem. Soc.* **2006**, *128*, 9882−9886.
(39) Lu, T.; Chen, F. Multiwfn: A Multifunctional Wavefunction Analyzer. *J. Comput. Chem.* **2012**, *33*, 580−592.
(40) Giannozzi, P.; Baroni, S.; Bonini, N.; Calandra, M.; Car, R.; Cavazzoni, C.; Ceresoli, D.; Chiarotti, G. L.; Cococcioni, M.; Dabo, I.; Dal Corso, A.; de Gironcoli, S.; Fabris, S.; Fratesi, G.; Gebauer, R.; Gerstmann, U.; Gougoussis, C.; Kokalj, A.; Lazzeri, M.; Martin-Samos, L.; Marzari, N.; Mauri, F.; Mazzarello, R.; Paolini, S.; Pasquarello, A.; Paulatto, L.; Sbraccia, C.; Scandolo, S.; Sclauzero, G.; Seitsonen, A. P.; Smogunov, A.; Umari, P.; Wentzcovitch, R. M. QUANTUM ESPRESSO: A Modular and Open-Source Software Project for Quantum of Materials. *J. Phys.: Condens. Matter* **2009**, *21*, No. 395502.
(41) Uemura, T.; Hirose, Y.; Uno, M.; Takimiya, K.; Takeya, J. Very High Mobility in Solution-Processed Organic Thin-Film Transistors of Highly Ordered [1]Benzothieno[3,2-b]Benzothiophene Derivatives. *Appl. Phys. Express* **2009**, *2*, No. 111501.
(42) Takimiya, K.; Shinamura, S.; Osaka, I.; Miyazaki, E. Thienoacene-Based Organic Semiconductors. *Adv. Mater.* **2011**, *23*, 4347−4370.

https://doi.org/10.1021/jacs.2c01357
J. Am. Chem. Soc. 2022, 144, 11159−11167